Additive manufacturing of high-strength and ductile high entropy alloy $CoCrFeNiW_{0.2}$ composites via laser powder bed fusion and post-annealing

Chee Koon Ng,[1*] Kewu Bai,[2*] Delvin Wuu,[1] Kwang Boon Lau,[1] Jing Jun Lee,[1] Augustine Kok Heng Cheong,[1] Fengxia Wei,[1] Baisong Cheng,[1] Pei Wang,[1,3*] Dennis Cheng Cheh Tan,[1] Yong-Wei Zhang[2]

[1]*Institute of Materials Research and Engineering, Agency for Science Technology and Research, 2 Fusionopolis Way, #08-03 Innovis, Singapore 138634, Republic of Singapore*

[2]*Institute of High Performance Computing, Agency for Science, Technology and Research, Fusionopolis Way, #16-16 Connexis, Singapore 138632, Republic of Singapore*

[3]*Engineering Cluster, Singapore Institute of Technology, 10 Dover Drive, Singapore 519961, Republic of Singapore*

Corresponding authors: ng_chee_koon@imre.a-star.edu.sg (C. K. N.), baikw@ihpc.a-star.edu.sg (K. B.), wangp@imre.a-star.edu.sg (P. W.)

Abstract:

A $CoCrFeNiW_{0.2}$ metal-matrix composite (MMC) was fabricated by laser powder bed fusion (LPBF) and post-annealing, which exhibited comparable tensile ductility (44%) and yield strength (385 MPa) to as-casted CoCrFeNiW high entropy alloys with much higher W concentration. An Integrated Computational Materials Engineering (ICME) framework coupled with thermo-kinetic simulations was built to investigate the microstructure evolution and mechanical response of the as-fabricated and post-annealed MMCs. The combination of strength and ductility of the MMC can be attributed to the synergistic combination of dislocation, solid solution and grain boundary strengthening due to the multiple roles of W in the LPBF and post-annealing processes.

Keywords: metal matrix composites, metals and alloys, laser processing, powder metallurgy, diffusion, microstructure

1. Introduction

The development of high entropy alloys (HEAs) using additive manufacturing has advanced rapidly and offers great promise in the manufacturing of geometrically complex parts with desirable properties [1]. Laser powder bed fusion (LPBF) is an additive manufacturing technique that uses a high-powered laser to selectively fuse successive layers of metal powders until the desired shape is produced. The feedstock powders used in LPBF of these alloys are usually pre-alloyed and hence the compositions of the powders are generally fixed. *In-situ* alloying is a strategy that allows for mixed powder feedstock to be used in LPBF and can be used to fabricate many different alloy compositions rapidly, which is extremely useful in the design of functional HEAs. This strategy had been mainly used for developing aluminum and titanium alloys and recently extended to HEAs owing to their superior mechanical properties such as the exceptional strength, ductility and fracture toughness at cryogenic temperatures [2]. One of the challenges of *in-situ* alloying, in the fabrication of alloys with constituents such as W with a large contrast in melting point and coefficient of thermal expansion (CTE), is the formation of the intermetallic phases and unmelted particles. In the literature, they are usually regarded as defects in the LPBF parts and are believed to be deleterious to mechanical properties. Interestingly, this phenomenon can be used to develop metal-matrix composites (MMC) with superior mechanical properties, where the thermal mismatch stress-induced dislocations were instead regarded as a strategy towards MMCs with high strength [3].

The first attempt to generate W-Ni MMC using LPBF was carried out by Zhang et al. [4], who investigated the forming mechanism of W-Ni particles in the alloy. Recently, Chen and co-workers fabricated W-Ni-Fe-Co composites by LPBF and investigated the effects of laser process parameters and chemical compositions on densification, microstructures, and tensile properties [5]. The most recent work was by Jäcklein's group, where the authors used LPBF to generate composite materials composed of an X3NiCoMoTi 18-9-5 maraging steel as matrix and spherical tungsten particles as filler material [6]. Although post-annealing is one of the most common post-processing methods for relieving large residual stress in LPBF parts, its effects on the microstructures and mechanical properties of the LPBF-processed HEAs and HEA-based MMCs were seldom reported [6, 7]. This is mainly due to a lack of comprehensive understanding of the intertwined metallurgical process in the post-annealing process of the MMCs including the diffusion between unmelted metal and matrix, interface layer formation, as well as the concurrent stress relaxation process.

In this study, we fabricated the $CoCrFeNiW_{0.2}$ HEA via *in-situ* alloying by mixing CoCrFeNi and W feedstock powders using the LPBF process. As a result, we obtained an MMC with an FCC matrix and unmelted W as filler particles. Post-annealing was performed due to the multiple roles of W in alloys in literature [8-11]. Due to the ultrafast heating and cooling rates (10^6 –10^8 K/s) in LPBF, it is well known that the as-built products contain excessive residual stress or dislocations which can be removed via a post-annealing process. On the other hand, the concentrated dislocations in the FCC matrix of as-fabricated (AF) sample may significantly promote the diffusion of remaining unmelted metal W into the HEA matrix to enhance the interface bonding and improve its ductility [8]. Furthermore, the unmelted W may act as heterogeneous nuclei to enhance nucleation rate and cause a change in shape and size of grains of the solidified HEAs. More importantly, the diffusion of W into the matrix can significantly suppress grain growth, which induces a uniform grain size distribution [9] and solid solution strengthening simultaneously. According to the Labush model [12], W may act as the ideal intrinsic strengthener of the matrix due to large lattice and modulus differences of W (1.549 Å, 161 GPa) compared to those of Co (1.385 Å, 75 GPa), Cr (1.423 Å, 76 GPa), Fe (1.428 Å, 82 GPa), and Ni (1.377 Å, 115 GPa) [10]. The incorporation of 3 at.% W into the as-cast ternary CoCrNi matrix increased its intrinsic strength by ∼20%, leading to a good combination of strength and ductility [10]. The as-cast $CoCrFeNiW_{0.4}$ alloy exhibited a yield strength of 315.6 MPa with a considerable ductility of 33.1%, which resulted from both solid solution strengthening in the FCC phase and precipitation strengthening due to the μ-phase precipitates. The as-annealed alloy exhibited a higher yield strength of 525.2 MPa with a ductility of 10.5% [13].

Via the post-annealing process at 1300 °C for 5 hours, $CoCrFeNiW_{0.2}$ formed an MMC comprising of a FCC matrix and μ phase particles. Remarkably, this HEA exhibits a ductility up to 44% and a yield strength of about 385 MPa, comparable to the mechanical properties of HEAs with higher W loadings, such as $CoFeFeNiW_{0.4}$. A good balance of strength and ductility was achieved for the LPBF-processed part via the different strengthening mechanisms of the MMC composite. These strengthening mechanisms were investigated via an Integrated Computational Materials Engineering (ICME) framework coupled computational thermodynamics.

2. Methodologies

2.1 Experimental

2.1.1 Alloys fabrication and post-annealing

The pure tungsten (W) powder (99.9%, <325 mesh) supplied by International Laboratory USA, and the nitrogen gas atomized CoCrFeNi powder with a particle size distribution of 15 – 45 μm from Vday Additive Manufacturing Technology Co. Ltd were used as raw materials. The nominal composition of CoCrFeNi was shown in Table 1. The as-fabricated $CoCrFeNiW_{0.2}$ (designated as AF) was prepared by LPBF via the following alloying strategy. Firstly, CoCrFeNi and tungsten powders were mixed in a 5:1 mole ratio (6.13 g CoCrFeNi: 1 g of W) and roll-milled at 150 rpm for 24 hours with the ball to mass ratio of 1:1. The mixed $CoCrFeNiW_{0.2}$ powders were then sieved and vacuum dried at 60°C overnight, which were further used to fabricate AF coupons using a Trumpf TruPrint 1000 system in an argon environment with oxygen content below 100 ppm. An initial set of experiments were used to optimize the processing parameters to minimize cracking and excessive porosity in the sample. The optimized parameters were determined to be: laser power (P) = 175 W, scanning speed (V) = 150 mm/s, hatching spacing (H) = 100 μm, layer thickness (L) = 30 μm, and a standard alternating x/y-raster scan pattern with 67° rotation between adjacent layers.

Table 1. Chemical composition of the CoCrFeNi powder.

Element	**Co**	**Cr**	**Ni**	**Fe**
Composition (at. %)	25.0	24.9	25.0	25.1

The AF samples were then annealed in a muffle furnace at 1300 °C at a heating rate of 6 °C/min for two different hold times, 0 h and 5 h. The 0 h and 5 h samples are denoted as HT1 (heat treatment 1) and HT2 (heat treatment 2) respectively. The AF, HT1 and HT2 coupons were sectioned along the longitudinal plane, mechanically grinded, and polished utilizing conventional metallurgical procedures down to 0.3 μm colloidal silica suspension followed by vibratory polishing (VibroMet 2) for further analysis.

2.1.2 Microstructural characterization

Microstructures of the samples were examined using Olympus BX53M optical microscope and JEOL JSM-7600F scanning electron microscope (SEM) coupled with energy dispersive spectroscopy (EDX) detectors for elemental analysis and mapping. Phase identification and analysis were performed at room temperature using a Bruker D8

Advance X-ray diffractometer with Cu K- α radiation. Electron backscattered diffraction (EBSD) was also used (JSM-IT500HR) to determine the grain size morphology, crystallographic orientation and texture of the 3D printed alloys. Nanoindentation hardness tests were performed on KLA Tenco's Nano Indenter® G200 system with a Berkovich indenter at room temperature at a loading rate of 0.6 mN s^{-1} and a peak load of 300 mN.

2.1.3 Mechanical testing

Tensile tests were performed along both the horizontal and vertical directions of each printed alloy sample with the gauge dimensions of 6 mm (length) × 2 mm (width) × 1 mm (thickness) prepared by wire cutting (Fig. 1). The testing was performed in an Instron 5569 machine fitted with a video extensometer at a constant crosshead velocity of 0.3 mm/min at room temperature. Five samples were tested to ensure reproducibility.

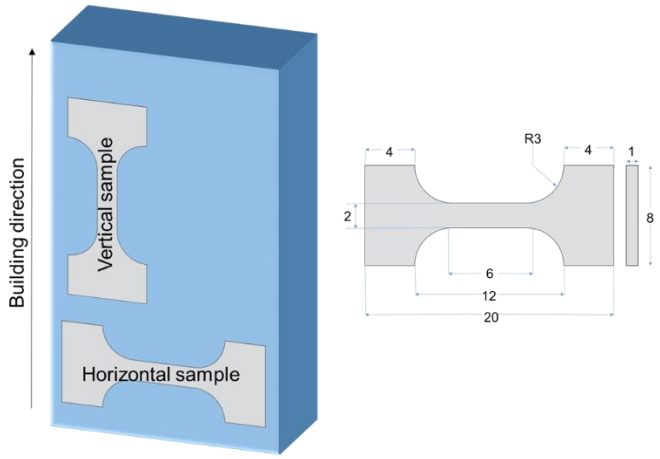

Fig. 1. Schematic illustration showing the horizontal and vertical tensile samples cut from the AF, HT1 and HT2 samples and their dimensions.

2.2 Theoretical modeling

2.2.1 Microstructure simulation by thermodynamic-kinetic modeling

Phase diagrams are an essential tool for studying phase evolution and transformation during solidification and annealing. Here, the TTNI8 database was used to provide a reliable theoretical base for understanding phase evolution in metallic composites. Using the thermodynamic database and the critically assessed diffusion model parameters, DICTRA software was found to be particularly suitable for solving diffusion problems and bringing new insights into the annealed microstructure evolutions of the $CoCrFeNiW_{0.2}$ system. With one-dimensional approximation, this software can be applied to simulate realistic microstructural evolutions in $CoCrFeNiW_{0.2}$, including diffusion profile between FCC matrix and the embedded W powders with different sizes, and precipitated or bonding phases under

both continuous heating process and subsequent isothermal annealing conditions. The main assumption in DICTRA is that equilibrium is maintained at the interface, which means that the concentrations at both sides of the interface are ruled by the phase diagram. The multicomponent diffusion equations in the various regions of the material are solved under this assumption. The kinetic model is briefly described in the supporting information. More details of the model can be found in references [14-16].

2.2.2 Strengthening prediction models coupled with DICTA simulation

Different strengthening mechanisms of HEAs were frequently reported in the literature [1]. One of the strengthening mechanisms is the friction stress of the lattice (σ_f) and unusual solid-solution strengthening (σ_{ss}) owing to the large lattice and modulus mismatch of constituents. Another is the grain boundary strengthening (σ_{GB}) induced by the extremely fast heating and cooling rates in the SLM process that usually generate a much smaller grain size compared with the casting process. The third one is the contribution of dislocation strengthening (σ_ρ) owing to the formation of the complex dislocation morphology in HEAs arising from either thermal cycles of LPBF or CTE mismatch. For the MMC HEAs, the loading effect (σ_l) arsing from the load-transfer from the matrix to the hard particle will strengthen the materials with good bonding between the matrix and second phases. Moreover, precipitation or dispersion hardening is one of the important strengthening mechanisms that can be quantified by Orowan stress (σ_{or}).

Similar to the pseudo-binary treatment of $CoCrFeNiM_x$ (M=Al, Ti and Mo) [17], we treated W as a solute in the solvent of CoCrFeNi. This means that the lattice parameter and shear modulus of CoCrFeNi with dilute doping of W can be, respectively, approximated by Vergard's law and the rule-of-mixture method as suggested by Varvenne and Curtin [18]. Since the ground state of W is not FCC, the calculated lattice parameter of W (a=4.043 Å) in FCC structure from first principles calculation [19] was used in the calculation together with those of CoCrFeNi [17]. In this case, the Labusch model [20] was usually used to describe the contribution to the total strength σ_{ss} caused by element W:

$$\sigma_{ss} = AG\epsilon {x_W}^{2/3} \quad (1)$$

where G is the shear modulus of the alloys, x_W is the mole fraction of element W, and A is a constant that is fitted with experimental data. $\varepsilon = \left(\frac{\epsilon_G}{1+0.5|\epsilon_G|^2} + \alpha^2 {\varepsilon_a}^2\right)^{\frac{2}{3}}$. ϵ_G and ϵ_a represent two contributors to the elastic interaction of a dislocation with the strain field of a single solute atom W. $\varepsilon_a = \frac{1}{a}\frac{da}{dx}$ denotes the lattice constant (a) mismatch. $\varepsilon_G =$

$\frac{1}{G}\frac{dG}{dx}$ denotes the shear modulus (G) mismatch. The dimensionless parameter (α= 16) describing the type of dislocations was used here. The grain-boundary strengthening is approximated by the well-known Hall–Petch equation:

$$\sigma_{GB} = \frac{k_{hp}}{\sqrt{d}} \quad (2)$$

where K_{hp} is the Hall–Petch coefficient and d is the grain size. The dislocation strengthening model is as follows:

$$\sigma_{\rho} = \alpha M G b \sqrt{\rho} \quad (3)$$

where α=0.2 is constant, M=3.06 is the Taylor factor for polycrystalline FCC matrix, G=84 GPa is the shear modulus of CoCrFeNi matrix, and b is the magnitude of Burgers vector (0.251 nm). ρ is the dislocation density [21]. The Orowan stress, σ_{Or}, of material with average particle spacing λ can be written as [21]:

$$\sigma_{Or} = M \frac{0.4Gb}{\pi\sqrt{1-\nu}} \frac{\ln(\frac{2\check{r}}{b})}{\lambda p} \quad (4)$$

$\check{r}$ is the mean radius of a circular cross-section in a random plane for a spherical precipitate, $\check{r}$= 2/3*r*, where *r* is the mean radius of the precipitates, λ_P is the edge-to-edge inter-precipitate spacing, and λ_P is given as follows [21]:

$$\lambda = 2r\sqrt{\frac{\pi}{4f}} - 1 \quad (5)$$

where *f* is the volume fraction of precipitates. In this case, the load sharing effect can be written as [22]:

$$\sigma_l = 0.5 f \sigma_a \quad (6)$$

where σ_a is the stress of matrix.

3. Results and Discussion

3.1 Microstructure analysis

Fig. 2 shows XRD patterns of the AF, HT1 and HT2 samples. It can be seen that the strong peaks of face centered cubic (FCC) structured solid solution are detected in all three samples. The diffraction peaks corresponding to W (PDF card #1–1203) were observed in those of AF and HT1 samples. It is worth noting that the weaker peaks corresponding to μ-W_6Fe_7 type phase (PDF card #02-1091 and #20-0538) are found in those of the post-annealed samples HT1 and HT2, which are supported by the magnified XRD spectra for HT1 (Fig. 2b and Fig. 2c) within a range of 35° – 50° and 66° – 83°, respectively. The results suggested that firstly, the AF sample is a metallic composite composed of FCC solid matrix and unmelted W particles, and secondly the high-temperature annealing of AF at 1300 °C may yield μ-phase precipitates accompanied with the elimination of unmelted W upon prolonged annealing.

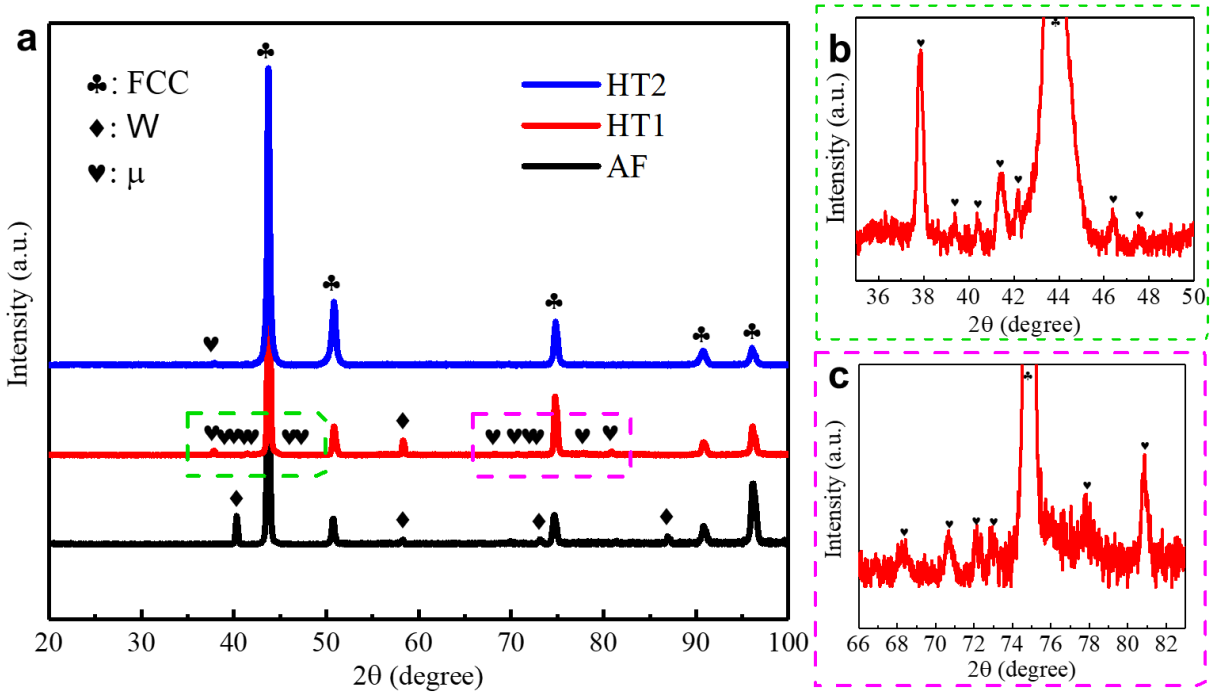

Fig. 2. (a) The full XRD spectra of AF, HT1 and HT2 HEAs, and (b), (c) the magnified spectra for the regions marked in (a), showing the details of some weak peaks corresponding to the μ phase.

The microstructures of AF, HT1 and HT2 are shown in Fig. 3. The SEM-EDX (Fig. 4, Table 2) results indicate that the bright particles in the AF sample correspond to unmelted W while the surrounding darker region corresponds to the FCC phase in agreement with XRD results shown in Fig. 2, although we cannot rule out the formation of a minor amount of μ phase owing to the detection limit of experimental techniques. The measured W concentration (3.7 at.%, Table 2) in the FCC matrix of AF implied that some W had dissolved into the matrix during the LPBF process. Upon annealing, HT1 shows two types of particles embedded in the darker FCC matrix, namely the core-shell and shell particles (Fig. 3b, inset). The core-shell particle consists of a pure W core, surrounded by W enriched (W content ~40 at. %) μ phase exterior shell, while the shell particle consists of only the W enriched μ phase (Table 2). These observations are corroborated by the XRD (Fig. 2), EDX mapping (Fig. 4e) and line scan results (Table S1). On prolonged annealing, the SEM image of HT2 shows only the μ phase shell particles embedded in the matrix, with also no detectable W diffraction peaks in the XRD. This indicates that W atom, which may be behaving like the case in filler particles in the brazing-like process, diffuses into FCC matrix via consuming itself to form the μ phase shell [23].

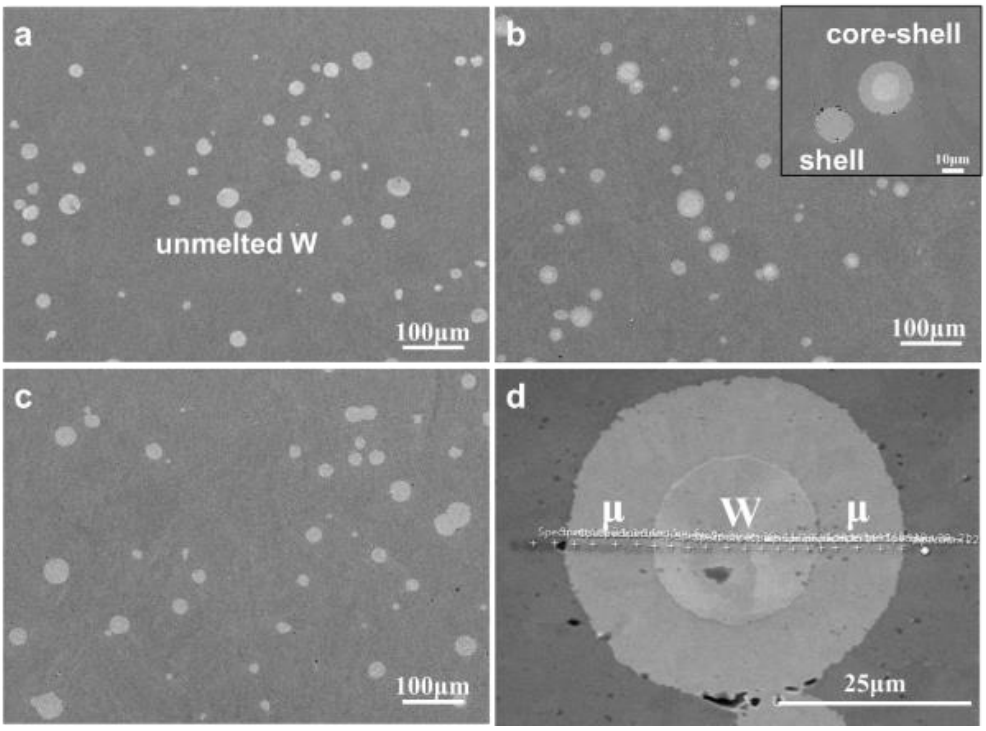

Fig. 3. SEM secondary electron image of the (a) AF, (b) HT1, and (c) HT2, showing unmelted W particles in the matrix in (a), core-shell and shell particles in (b) and shell particles in (c). The core-shell and shell particles in HT1 is highlighted in the insert of (b). (d) SEM micrographs and EDS line scan results for typical cross-sections of core-shell in HT1. The light-grey points in the figure show the line scan trace.

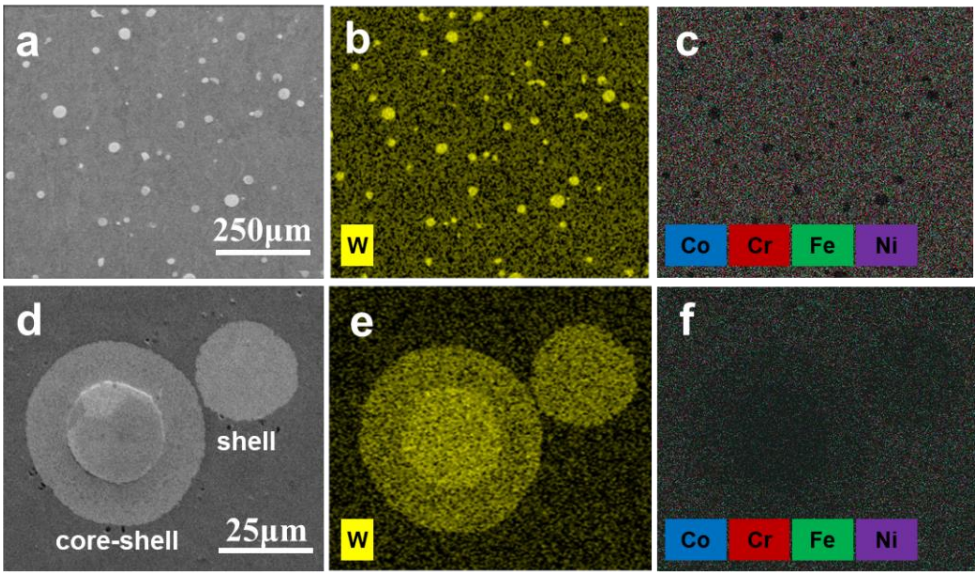

Fig. 4. (a), (d) SEM secondary electron image of AF and HT1 samples respectively. Micrographs in (a) and (d) were examined using EDX elemental mapping of W, Co, Cr, Fe and Ni in (b), (c), (e) and (f).

Table 2. Chemical compositions (in at.%) of different regions in AF, HT1 and HT2 samples.

Alloy	Region	Co	Cr	Fe	Ni	W
AF	Matrix	23.80	24.40	24.50	23.60	3.70
	Particles	-	-	-	-	100
HT1	Matrix	24.53	23.73	23.95	23.78	4.03
	Core	-	-	-	-	100
	Shell	18.04	16.46	15.00	9.78	40.70
HT2	Matrix	24.35	23.20	24.08	23.65	4.73
	Shell	19.44	16.80	14.84	9.08	39.90

To further examine the microstructure of the samples, in particular the core-shell structure in HT1, EBSD was performed. Fig. 5 shows the phase maps and inverse pole figures (IPF) of the three samples. The core-shell structure in HT1 consists of a pure W core in blue, surrounded by a W-enriched shell in the μ phase in yellow (Fig. 5a). HT1 also contains shell particles that consists of only the W-enriched shell in the μ phase (Fig. 5b). These particles are embedded in the FCC matrix in red. Moreover, the μ phase has an average grain size of 1.3 μm in HT1 that increases slightly to 1.5 μm in HT2 upon prolonged annealing. The small grain size of the μ phase is likely due to its high precipitation driving force when the AF sample was annealed at a high temperature. A closer look at the grain boundaries of the core-shell particles of the HT1 (Fig. S2) in EBSD indicated that there existed a large amount of twins within the fine μ phase grains. The exact cause of the twin formation in the intermetallic layer is not clear. Kumar [24] argued that these twins might be due to the large mismatch in the coefficient of thermal expansion of the W and FCC matrix. The mismatch would have induced strain and consequently, caused mechanical twins to form in the growing reaction layer. Similar microstructure with numerous twins found inside the μ phase with small grain sizes (about 1 μm) have also been observed in the 1200°C/500hours diffusion annealed composite composed of 316 steel and W wires [24].

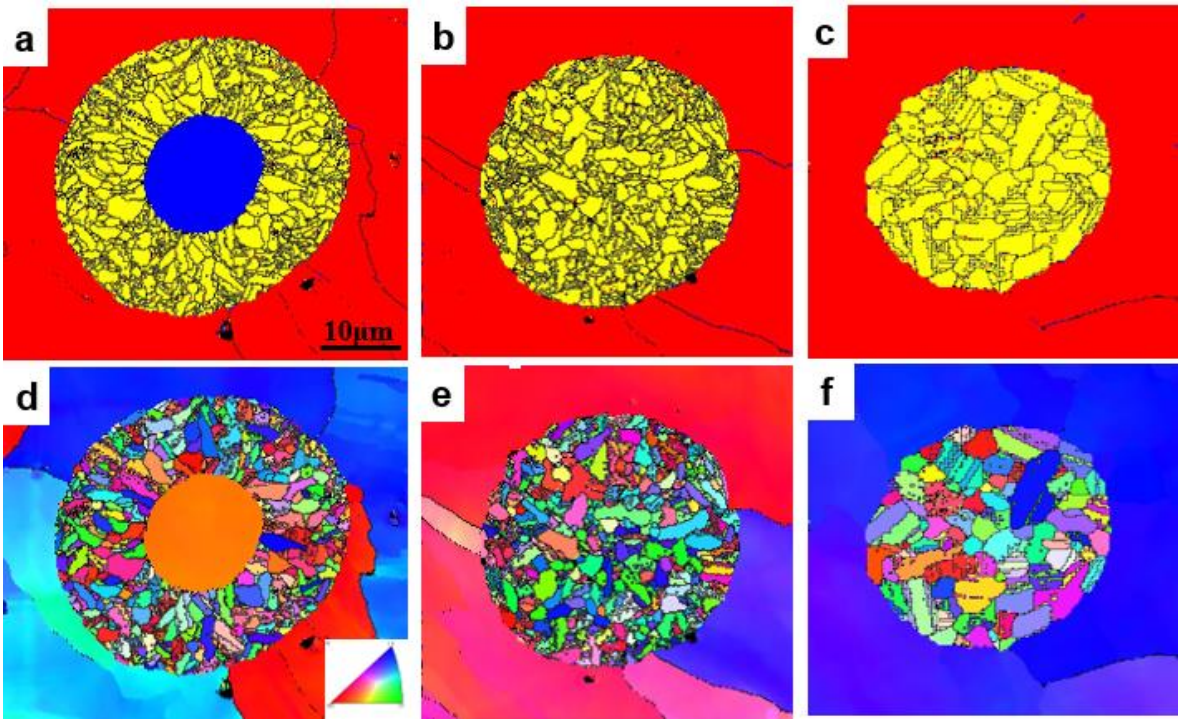

Fig. 5. The EBSD phase map (top) and corresponding IPF maps (bottom). (a), (d): HT1 core-shell particles, (b), (e): HT1 shell particles and (c), (f): HT2 shell particles. In the EBSD maps: red – FCC, blue – unmelted tungsten, and yellow – μ phase for phase map.

Fig. 6 shows the IPF maps of AF, HT1 and HT2 at the vertical and horizontal build directions and the derived grain sizes of these samples are shown in Table 3. The grain sizes of our LPBF-built CoCrFeNiW samples in both build directions are more uniform than the previously built CoCrFeNi with the extraordinarily large columnar grain sizes of ~ 3 mm in length and ~ 200 μm in width [25]. The unmelted W presumably acted as a nucleating agent which facilitated heterogeneous nucleation in the LPBF process, reducing the grain anisotropy in the built samples [11]. Furthermore, post-annealing does not result in grain coarsening or significant changes in the grain shape. Instead, there is a more uniform grain distribution in HT2 for both build directions. This is likely due to the partial dissolving and subsequent diffusion of W into the FCC matrix, where W can significantly suppress grain growth and induce a more uniform grain size distribution during the annealing process [9]. The strong <110> texture along the building direction can be attributed to thermal gradient of the LPBF process, which results in a narrower and deeper melt pool that favours the formation of <110> crystallographic textures [26]. It has been reported that strong texturing along <110> can lead to higher strength and ductility compared to <100> in FCC alloys [27, 28], which might be one of the reasons for the higher σ_{YS} and σ_{UTS} for the horizontal samples. Due to the columnar grain formation, the mean free

pathway for dislocation to transverse before stopping by a cell boundary is longer along the building direction than horizontal direction, irrespective of <110> or <100> texturing [26]. According to the Hall-Petch effect, vertical samples experience longer mean free pathway under tensile, and show smaller σ_{YS} and σ_{UTS} but higher ductility than horizontal samples.

3.2 Mechanical properties

Room temperature nano-indentation was performed on HT2 to ascertain the nano-hardness of the μ phase shell particles and the FCC matrix. 25 points were indented on the shell particles and 25 points (5 x 5 grid) were indented on the FCC matrix. The average hardness of the μ phase particles was 16.69 GPa, which was consistent with the reported hardness of topologically close-packed (TCP) μ particles [29, 30], while the average hardness of the FCC matrix was 3.08 GPa (Table S3). This data also shows that the μ particles are much harder than the surrounding FCC matrix.

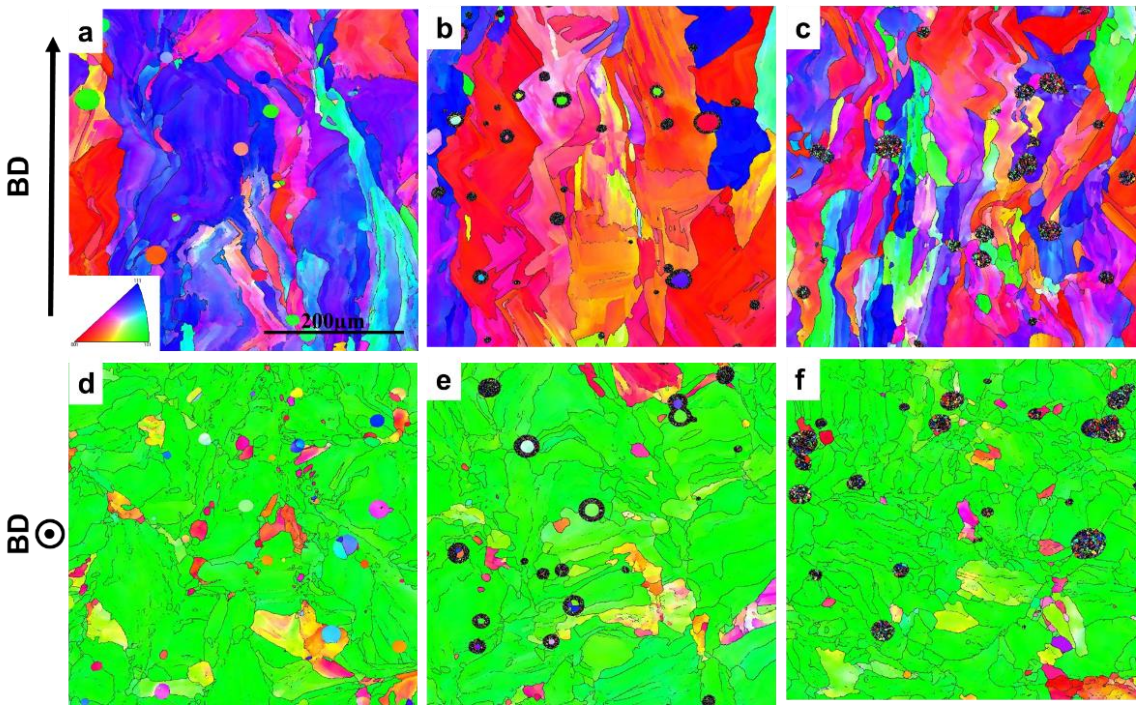

Fig. 6. The EBSD IPF Z maps of (a, d) AF, (b, e) HT1, and (c, f) HT2 samples. The top row (a, b, c) represent side planes while the bottom row (d, e, f) represent top planes.

Table 3. The area-weighted grain size [31] of AF, HT1 and HT2 samples derived from Fig. 6. "H" and "V" represent horizontal and vertical samples, respectively.

Sample	Grain size/μm
AF H	152.6
HT1 H	112.8
HT2 H	92.6
AF V	245.3
HT1 V	200.7
HT2 V	100.7

Fig. 7a and 7b shows the tensile stress-strain curves for the samples printed in the horizontal and vertical build directions. The build direction and the duration of annealing strongly affected yield strength σ_{YS}, ultimate tensile strength σ_{UTS} and ductility. As mentioned above, all the samples exhibited higher σ_{UTS} but lower ductility in the horizontal direction as compared to the vertical direction (Table 4). This is in agreement with several previous studies [26, 32-35] that indicated that the build direction of additively manufactured (AM) samples has a strong effect on their strength, with samples that are loaded parallel to the build direction (vertical samples) having lower strength values. Wang et al. [34] and Mukherjee [35] also attributed the anisotropic tensile properties to the elongated (columnar) grain structures in AM samples with respect to the loading direction. In the vertical samples, the grains are oriented parallel to the loading direction and the mean free path available for dislocation movement is higher. Thus, the dislocations have to cross lesser grain boundaries, which act as barriers to dislocation movement, resulting in lower strengths and vice versa. Fig. 7c and 7d shows the strain hardening and true stress-strain curves for these samples. The samples show similar strain hardening responses, with HT2 showing the highest strain hardening rate, followed by HT1 then AF. This may be associated with the different grain sizes (Table 3), the precipitated μ phase amounts, as well as the increasing W content from AF to HT2. These factors may increase the dislocation motion resistance and hardening rates consequently. These observations are consistent with the CoCrNiW medium entropy alloys reported by Yin's group [36].

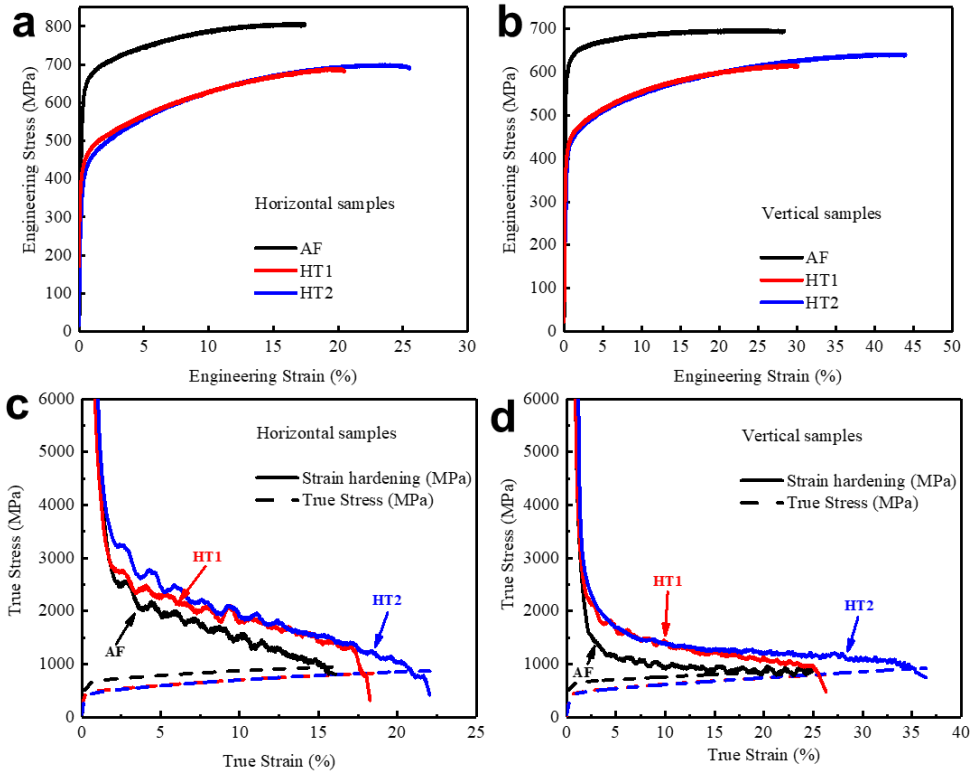

Fig. 7. Tensile engineering stress-strain curves of (a) horizontal samples and (b) vertical samples. Strain hardening curves and true stress-strain curves of (c) horizontal samples and (d) vertical samples.

Table 4. Yield strength (YS), ultimate tensile strength (UTS) and uniform ductility of tensile samples from Fig. 7. "H" and "V" represent horizontal and vertical samples, respectively.

Alloy	Yield strength, σ_{YS} (MPa)	Ultimate tensile strength, σ_{UTS} (MPa)	Uniform Ductility (%)
AF H	610 ± 15	814 ± 9	17 ± 1
HT1 H	407 ± 12	690 ± 10	20 ± 1
HT2 H	406 ± 16	721 ± 15	26 ± 1
AF V	540 ± 63	699 ± 10	28 ± 5
HT1 V	408 ± 14	624 ± 7	30 ± 2
HT2 V	384 ± 25	646 ± 7	44 ± 4

The horizontal AF has a relatively high σ_{YS} and σ_{UTS} of 610 MPa and 814 MPa, respectively, with a ductility of 17%. Upon annealing, the σ_{UTS} of HT1 drops slightly accompanied by a corresponding increase in ductility as compared to AF. On prolonged annealing, both σ_{UTS} and ductility of HT2 increase compared to HT1, resulting in a σ_{UTS} of 721 MPa and ductility of 26%. The vertical samples also exhibit similar trends and the vertical HT2 shows an extremely good ductility of 44%, with a σ_{UTS} of 646 MPa. All our 3D-printed alloys show much higher σ_{YS} and σ_{UTS} compared to the reported as-cast $CoCrFeNiW_{0.2}$ alloys [13].

The fracture morphologies of the samples after tensile testing (Fig. 8) may help explain their mechanical property variations. The fracture surfaces of all the samples are dominated by near-equiaxed small dimples in the matrix (Fig. 8g, h, i), which indicates ductile fracture with severe plastic deformation during the tensile experiments. However, the dimples in AF are large but shallow with fewer tearing edges indicating lower ductility (Fig. 8g red circles), whereas the dimples for HT2 are small and deep, with larger tearing edges, which indicate higher ductility (Fig. 8i) [37]. Cracks were observed in the unmelted W particles in AF (Fig. 8d), which suggested that the interface bonding between W and FCC matrix is strong enough to allow load transfer from the matrix to the W particle in order to promote composite strengthening. Deep cracks were also observed at the interface of the W core and μ shell in HT1 (Fig. 8e), indicating that the thermal stress arising from the CTE mismatch between different layers could not be accommodated by the brittle μ shell layer. This resulted in the lowest σ_{UTS} in HT1 among the three samples. In contrast, no cracks were observed at the interface between the μ shell particles and FCC matrix in HT2 (Fig. 8f), which indicated the higher interface binding strength due to extended diffusion of the W into the matrix. This explains why HT2 exhibits a good combination of strength and ductility amongst the three samples.

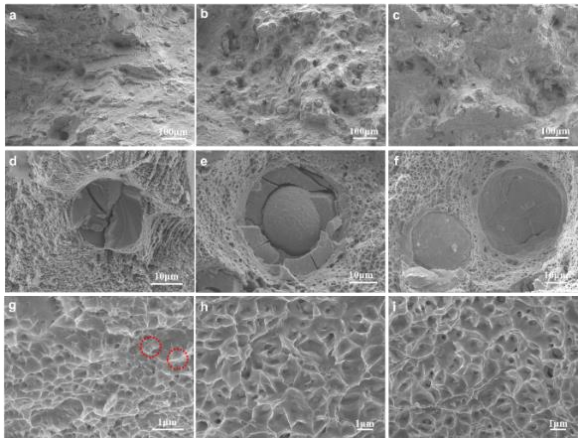

Fig. 8. The tensile fracture morphologies of the horizontal samples AF (a, d, g), HT1 (b, e, h) and HT2 (c, f, i).

3.3 Multiple strengthening mechanisms in AF, HT1, and HT2

In order to elucidate the strengthening mechanisms in AF, HT1 and HT2, the ICME framework previously mentioned in section 2 was used. As a benchmark, we first predicted the σ_{YS} of as-cast $CoCrFeNiW_x$ [13] with a grain size of 300 μm (Fig. 9a). The constant k_{HP} (954 MPa m^{-2}) and A (2.85×10^{-3}) in equation 12 were fitted with the σ_{YS} of as-cast CoCrFeNi and as-cast $CoCrFeNiW_{0.2}$ composed of a single FCC phase (5.5 at.% W). The optimized parameters were further used to predict the σ_{YS} of as-cast $CoCrFeNiW_{0.4}$ composed of FCC (8.37 at.% W) and μ phases. Similar to the study on the strengthening mechanism of as-cast HEAs in the literature [8], the different contributions to the σ_{YS} of as-cast $CoCrFeNiW_{0.4}$ were highlighted by the stacked bars in varying colors. The fitted k_{HP} is close to the reported value (854 MPa m^{-2}) by Wu et al. [38] considering the uncertainty associated with the tensile test. Using the estimated volume fraction of μ phase (~0.1) from the optical microscopy in [13], we can see that the predicted σ_{YS} of $CoCrFeNiW_{0.4}$ is in good agreement with experimental data [13].

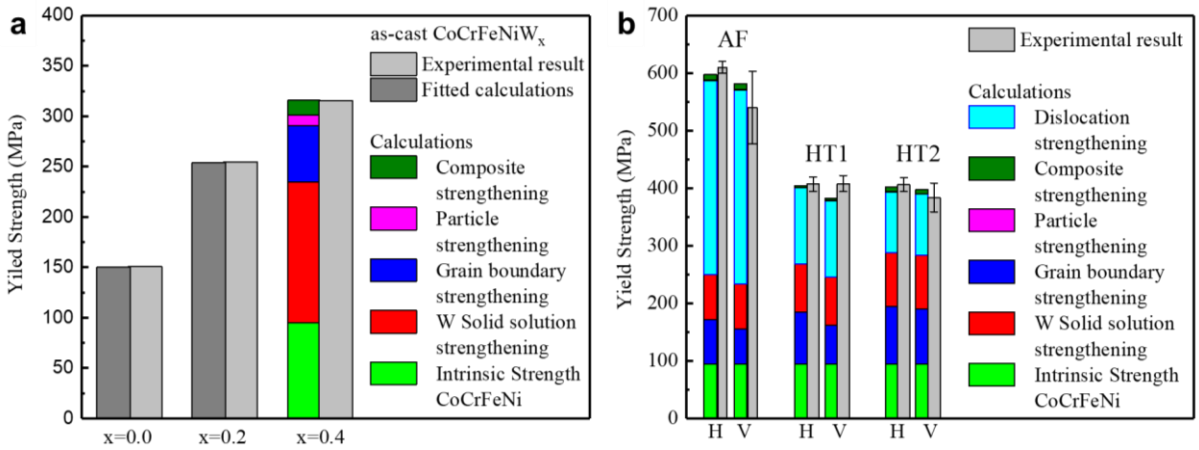

Fig. 9. Calculated and experimental yield strength, σ_{YS} of (a) as-casted $CoCrFeNiW_x$ [13] compared with our samples (b) AF, HT1 and HT2. H denotes horizontal samples and V denotes vertical samples. The different colors in the figures represent the contributions from different strengthening mechanisms: including the load-bearing effect (composite strengthening), solid solution strengthening, dislocation strengthening, Hall-Petch effect (grain boundary strengthening) and Orowan mechanism (particle strengthening).

Next, we turn to the calculation of σ_{YS} of AF and HT1 in both horizontal and vertical directions using different strengthening models (Fig. 9b). In this calculation, the average grain sizes of AF and HT1 in Table 3 were used. The concentration of W in the AF matrix measured by EDX is 3.7 at.% (Table 1). The volume fraction and mean diameters

of unmelted W in AF, estimated from quantitative image and SEM analysis (Fig. S4), are 0.033 and 17.76 μm, respectively. Similarly, the mean diameter of the particles in the HT1 structure was estimated as 17.80 μm. The effective volume of particle strengthening of HT1 was estimated as 0.016 considering the low interface strength between the W and the μ phase in the core-shell particles (Fig. 8e) and the concentration of W in the HT1 matrix was determined to be 4.03 at.% (Table 1). In this case, the corresponding dislocation density ρ of FCC matrix was estimated to be up to 6.8×10^{14} m^{-2} and 1.05×10^{14} m^{-2} for AF and HT1 based on experimental σ_{YS}. These results are consistent with the observation that the complex thermal cycle with a cooling rate of above 10^6 K s^{-1} in LPBF may generate high dislocation density, while post-annealing lowers the dislocation density [8]. Notably, the derived high dislocation density of AF is of the same magnitude as in $Al_{0.3}$CoCrFeNi (4×10^{14} m^{-2}) by LPBF [39]. The derived smaller dislocation densities in HT1 are about an order of magnitude larger than that annealed CoCrFeNi samples by LPBF (1573 K for 2 h, 2.18×10^{13} m^{-2}) [40]. This is in agreement with the observed dislocation density variation trend in the 1%C-CoCrFeMnNi HEA with heat treatment [7]. Fig. 9b also shows the calculated σ_{YS} of HT2 using the estimated volume fraction (0.0351) and the mean diameter of μ phase particles (20.75 μm) in HT2. The derived dislocation density in HT2 continues to decrease to 7.2 $x10^{13}$ m^{-2} upon prolonged annealing accompanied by the increase in the concentration of W (4.73 at. %) in the FCC matrix.

As can be seen from Table 5 and Fig. 9b, the main contribution to the strengthening mechanism for AF was dislocation strengthening due to the high dislocation densities resulting from LPBF processes. The contribution of the dislocation strengthening decreases upon post-annealing. Thus, in HT1 and HT2, solid solution strengthening and grain boundary strengthening contribute to a larger extent to the σ_{YS} as compared to the AF samples. The increase in the contribution of the solid solution strengthening is due to the increase in the W content upon annealing as W starts to diffuse from the particles to the FCC matrix. The increase in W content in the matrix also significantly suppresses grain growth and induces a more uniform grain size distribution which contributes to grain boundary strengthening [9]. The contributions of particle strengthening and composite strengthening are insignificant in all the samples due to small volume fraction and large particle size in the MMCs. In order to increase the contribution of particle and composite strengthening, the W concentration can be increased or the W particle size can be decreased during the fabrication process.

Table 5. Contributions of different strengthening mechanisms (in %) to the σ_{YS} of AF, HT1 and HT2 in the horizontal (H) and vertical (V) build directions.

Sample	Intrinsic strength	Grain boundary strengthening	Solid solution strengthening	Dislocation strengthening	Particle strengthening	Composite strengthening
AF H	15.7	12.9	13.2	56.3	0.3	1.6
AF V	16.2	10.5	13.5	57.9	0.3	1.6
HT1 H	23.5	22.2	20.6	32.7	0.3	0.8
HT1 V	24.8	17.6	21.9	34.6	0.3	0.8
HT2 H	23.6	24.7	23.3	26.5	0.2	1.7
HT2 V	23.9	23.9	23.5	26.8	0.2	1.7

Next, kinetic simulations will be utilized to demonstrate how the high dislocation density in the matrix promotes the W diffusion into the FCC matrix via μ layer, leading to the increase of the W concentration in the matrix. This enhances solid solution strengthening and modulates the grain size simultaneously, accounting for the good combination of strength and ductility in the HT2 sample, particularly in the horizontal build direction.

3.4 Diffusion process simulation coupled with stress relaxation

Kinetic simulations were performed to simulate the core-shell formation and W dissolving in the alloy system using the DICTRA software. Coupled with stress relaxation, the diffusion of W in the CoCrFeNi was investigated given its importance in modulating the microstructure and mechanical proprieties of the samples. For this purpose, a diffusion mobility database of the Co-Cr-Fe-Ni-W system was established. The diffusion data of FCC phases by Vaidya et al. [41] and Gaertherner et al. [42], one of the most reliable ones amongst all diffusion studies in HEAs [43], were used in a combination with the comprehensive computational and experimental kinetic study by Zhang et al. [44]. Meanwhile, the diffusion data of the BCC_A2 phase from references [45-47] were also used. Specifically, the diffusion model parameters of μ phase were assessed and evaluated with a $Co_{75}Ni_{25}$-W diffusion couple experiment at 1473 K (Fig. 10a) [48], and a core (W)-shell (μ) like structure along the radial direction of a 316 stainless steel matrix with embedded W wire that was heat-treated at 1473 k for 500 hrs (Fig. 10b) [24]. Consistent with experimental data, the grain size of μ phase was set as 1 μm, and model parameter F_{redGB}=0.565 (in equation 2) was used in the simulation of diffusion between 316 stainless steel matrix with embedded W wire. Table S4 shows the optimized diffusion mobility parameters of μ phase with typical stoichiometry A7B6.

For the kinetic simulation of the core-shell and shell formation in the post-annealing process, the grain size of the formed μ layer upon annealing was set as 1.3 μm, which is consistent with our EBSD experimental data. Considering the slow diffusion kinetics below 1073 K, the initial diffusion temperature was set as 1073 K with a heating rate of 6 K/min. Consistent with the derived dislocation densities in the yield strength prediction, the dislocation density in the FCC matrix was set as 6.8×10^{14} m^{-2} at 1073 K, which decreases to 1.05×10^{14} m^{-2} when it is heated to 1573 K, and further decreases to 7.2×10^{13} m^{-2} when it is annealed at 1573 K for 5 hrs.

To reproduce that diffusion profile across the dispersed particle in HT1 and HT2 using the assessed kinetic model parameters, an additional mobility enhancement factor (1.2) for Co, Cr, Fe and Ni in μ phase has to be used. Fig. 10c and 10d show the simulated diffusion profile in the core (W)–shell (μ) structure of HT1 and shell (μ) structure in HT2, respectively, in comparison with the EDX line scan results (Tables S1 and S2). The calculated concentration profiles for all five constituents (Co, Cr, Fe, Ni, and W) were in reasonable agreement with experimental data.

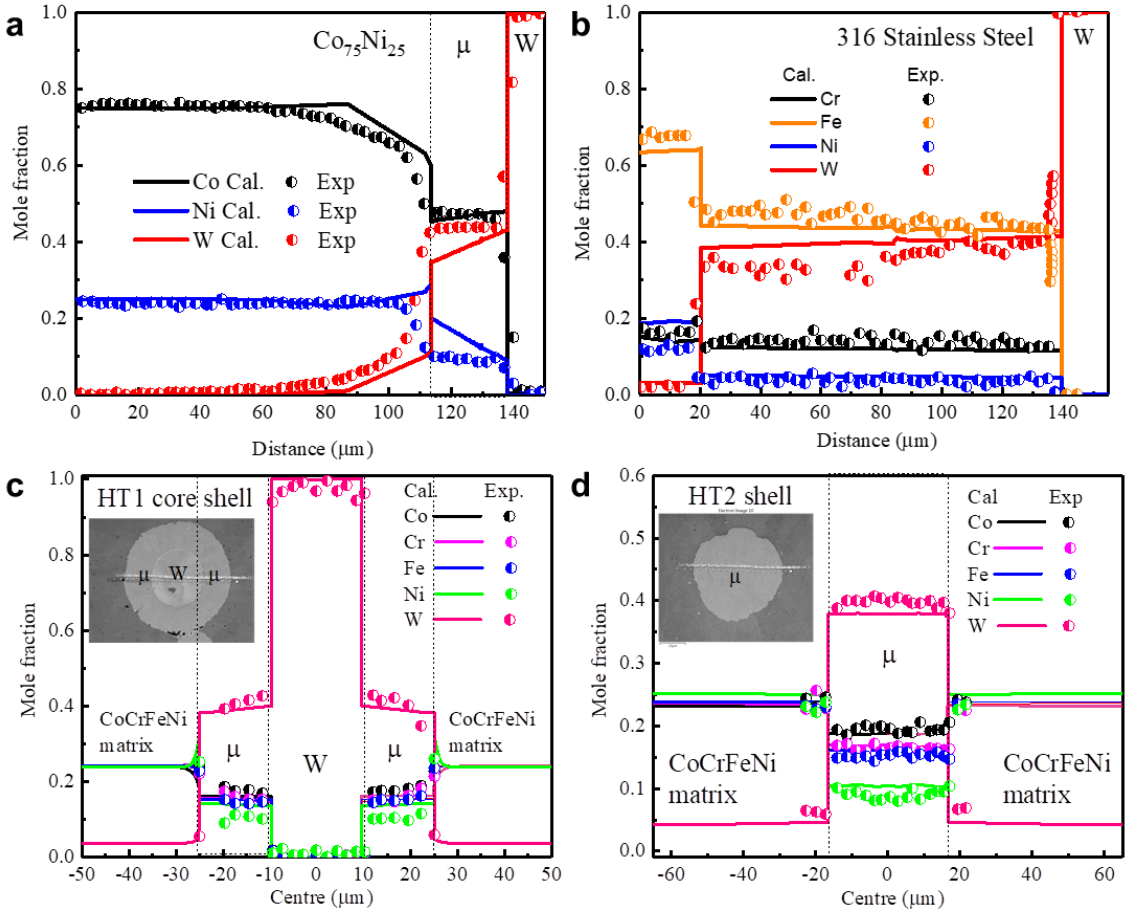

Fig. 10. Calculated (Cal.) and experimental (Exp.) one-dimensional diffusion profiles of $Co_{75}Ni_{25}$-W diffusion couple annealed at 1473K for 25 hrs [48]. (b) One-dimensional diffusion profiles of 316 steel-W wire annealed at 1473K for

500 hrs [24]. (c) One-dimensional (radial) diffusion profile across the core (W) shell (μ) particle of HT1 as measured by the SEM-EDX line in the insert. (d) One-dimensional (radial) diffusion profiles of HT2 across the light-grey μ particle. The white dotted lines in the insert of Fig. 10c and 10d denote SEM-EDX line scanning trajectory.

After validation with the experimental data, we predicted the diffusion profile of W by assuming that the unmelted W has the average radius of 8.88 μm in the AF. Fig. 11a and 11b shows the calculated W concentration in the half-cross section of HT1 and HT2 samples with core (W)-shell (μ) and μ shell particle, respectively. We calculated the diffusion profile of W in the matrix of HT2 without taking the dislocation density change into account, which is highlighted in Fig. 11c in red line compared with the calculation result coupled with dislocation during post-annealing in blue. It can be seen that the effective W concentration increases slightly in the matrix of HT1 in comparison with AF (3.7 at.%), but increases to about 4.62 at.% in the FCC matrix of HT2 owing to the diffusion process at 1573 K for 5 hrs. The predicted effective concentration is close to our EDX results (Table 2) despite the simplicity of the kinetic model. This demonstrates that the dislocations arising from the LPBF process significantly accelerate the diffusion of W into the FCC matrix.

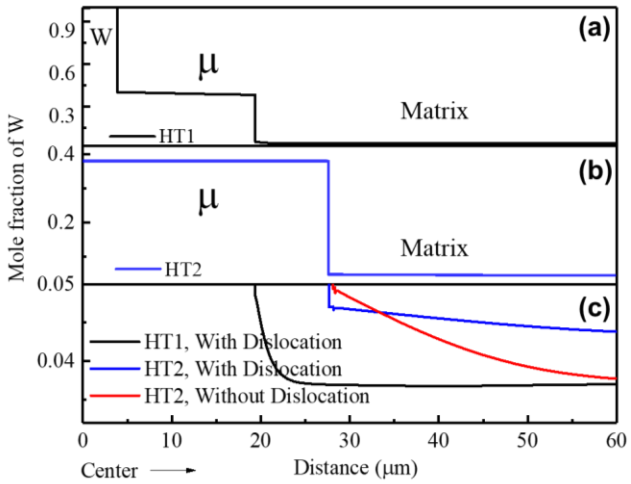

Fig. 11. Calculated diffusion profiles in the half cross-section of (a) the core (W)–shell (μ) particle and FCC matrix in HT1, and (b) μ phase shell particles and FCC matrix in HT2. The results from HT1 and HT2 with dislocation densities are highlighted as black and blue lines in (c) in comparison with the calculated red line without considering dislocation density.

It should be mentioned that a few simplifications in the built ICME framework might not be fully consistent with the complex microstructure of MMC. For example, the dislocations density and grain size are not fully uniformly distributed in the MMC, the particle and grain shapes are not perfectly spherical, and a special mixed rule of the grain

boundary diffusion and bulk diffusion was assumed. Despite these limitations, the established ICME framework provides meaningful predictions on the post-annealing of MMC with unmelted particles, in particular for MMC fabricated by LPBF. For $CoCrFeNiW_{0.2}$, the post-annealing alters the phase equilibrium that leads to the formation of the μ phase as a dispersed phase in the FCC matrix. From the strengthening models, an increase in the dispersed μ phase volume with increased W addition or a decrease in the W particle size may result in improved mechanical properties for the MMC. The multiple roles of W in the post-annealing process reasonably explain the microstructure evolution and account for the corresponding mechanical variations of the MMC. In particular, the developed model parameters pave a new way to design the LPBF-processed MMCs with unmelted metals and other base alloy matrices.

4. Conclusion

A $CoCrFeNiW_{0.2}$ MMC reinforced by W-containing μ phase particles was prepared via *in-situ* alloying of a mixture of CoCrFeNi and W powders using LPBF. The μ phase particles were formed by the diffusion of the unmelted W into the FCC matrix via post-annealing. The microstructure evolution, mechanical properties, and deformation behavior of the as-fabricated and post-annealed alloys were investigated. Under post-annealing conditions of 1300 °C for 5 h, the MMC exhibits a ductility of up to 44%, and a yield strength of about 385 MPa, which are comparable to those mechanical properties of eutectic alloys with higher W loadings, e.g. $CoFeFeNiW_{0.4}$. The balance in strength and ductility in these samples can be attributed to the dissolving of W into the FCC matrix. The unmelted W diffuses into the FCC matrix, resulting in solid solution strengthening, grain size homogenization and μ particle formation in the matrix. Based on the ICME analysis, the high yield strength in the MMC is found to arise from the synergistic combination of dislocation strengthening, solid solution strengthening and grain boundary strengthening. Our current work presents a new pathway to leverage on LPBF to fabricate MMCs by controlling unmelted metal powders and base alloys.

Acknowledgments

This work was supported by the funding from Agency for Science, Technology and Research (A*STAR) of Singapore via the Accelerated Materials Development for Manufacturing Programme (No. A1898b0043). The authors gratefully thank the technical support on nano-indentation analysis from Mr. Tzee Luai Meng of IMRE. DICTRA software was used in the kinetic simulations in the alloy system.

Declaration of Competing Interest:

The authors declare that they have no known competing financial interests or personal relationships that could have appeared to influence the work reported in this paper.

CRediT authorship contribution statement:

Chee Koon Ng: Conceptualization, Methodology, Validation, Investigation, Visualization, Data Curation, Writing – original draft. **Kewu Bai:** Methodology, Validation, Visualization, Data Curation, Software, Writing – original draft. **Delvin Wuu:** Investigation. **Kwang Boon Lau:** Investigation. **Jing Jun Lee:** Investigation. **Augustine Kok Heng Cheong:** Investigation. **Fengxia Wei:** Investigation. **Baisong Cheng:** Investigation, Writing – review & editing. **Pei Wang:** Conceptualization, Methodology, Resources, Formal analysis, Supervision, Project administration, Writing – review & editing. **Dennis Cheng Cheh Tan:** Funding acquisition, Writing – review & editing. **Yong-Wei Zhang:** Funding acquisition, Writing – review & editing.

Data availability

The data used to support the findings of this study are available from the corresponding author upon request.

References

[1] Han C, Fang Q, Shi Y, Tor SB, Chua CK, Zhou K. Recent Advances on High-Entropy Alloys for 3D Printing. Adv Mater. 2020;32(26):1903855.

[2] Sing SL, Huang S, Goh GD, Goh GL, Tey CF, Tan JHK, et al. Emerging metallic systems for additive manufacturing: In-situ alloying and multi-metal processing in laser powder bed fusion. Prog Mater Sci. 2021;119:100795.

[3] Hou YN, Yang KM, Song J, Wang H, Liu Y, Fan TX. A crystal plasticity model for metal matrix composites considering thermal mismatch stress induced dislocations and twins. Sci Rep. 2021;11(1):16053.
[4] Zhang DQ, Liu ZH, Cai QZ, Liu JH, Chua CK. Influence of Ni content on microstructure of W–Ni alloy produced by selective laser melting. Int J Refract Met Hard Mater. 2014;45:15-22.
[5] Chen H, Zi X, Han Y, Dong J, Liu S, Chen C. Microstructure and mechanical properties of additive manufactured W-Ni-Fe-Co composite produced by selective laser melting. Int J Refract Met Hard Mater. 2020;86:105111.
[6] Jäcklein M, Pfaff A, Hoschke K. Developing Tungsten-Filled Metal Matrix Composite Materials Using Laser Powder Bed Fusion. Appl Sci. 2020;10(24):8869.
[7] Park JM, Kim ES, Kwon H, Sathiyamoorthi P, Kim KT, Yu J-H, et al. Effect of heat treatment on microstructural heterogeneity and mechanical properties of 1%C-CoCrFeMnNi alloy fabricated by selective laser melting. Addit Manuf. 2021;47:102283.
[8] Zhang C, Zhu J, Zheng H, Li H, Liu S, Cheng GJ. A review on microstructures and properties of high entropy alloys manufactured by selective laser melting. Int J Extreme Manuf. 2020;2(3):032003.
[9] Jinlong L, Zhuqing W, Tongxiang L, Suzuki K, Hideo M. Effect of tungsten on microstructures of annealed electrodeposited Ni-W alloy and its corrosion resistance. Surf Coat Technol. 2018;337:516-24.
[10] Wu Z, Guo W, Jin K, Poplawsky JD, Gao Y, Bei H. Enhanced strength and ductility of a tungsten-doped CoCrNi medium-entropy alloy. J Mater Res. 2018;33(19):3301-9.
[11] Malatji N, Lengopeng T, Pityana S, Popoola API. Microstructural, mechanical and electrochemical properties of AlCrFeCuNiWx high entropy alloys. J Mater Res Technol. 2021;11:1594-603.
[12] Poletti MG, Fiore G, Gili F, Mangherini D, Battezzati L. Development of a new high entropy alloy for wear resistance: FeCoCrNiW0.3 and FeCoCrNiW0.3+5at.% of C. Mater Des. 2017;115:247-54.
[13] Wang L, Wang L, Tang Y, Luo L, Luo L, Su Y, et al. Microstructure and mechanical properties of CoCrFeNiWx high entropy alloys reinforced by μ phase particles. J Alloys Compd. 2020;843:155997.
[14] Bai K, Wu P. Assessment of the Zn–Fe–Al system for kinetic study of galvanizing. J Alloys Compd. 2002;347(1):156-64.
[15] Ågren J. Numerical treatment of diffusional reactions in multicomponent alloys. J Phys Chem Solids. 1982;43(4):385-91.
[16] Diffusion Module (DICTRA) Documentation Set, Thermo-Calc Version 2021b. https://thermocalc.com/content/uploads/Documentation/Current_Static/diffusion-module-dictra-documentation-set.pdf.
[17] Li X, Li Z, Wu Z, Zhao S, Zhang W, Bei H, et al. Strengthening in Al-, Mo- or Ti-doped CoCrFeNi high entropy alloys: A parallel comparison. J Mater Sci Technol. 2021;94:264-74.

[18] Varvenne C, Curtin WA. Strengthening of high entropy alloys by dilute solute additions: CoCrFeNiAl x and CoCrFeNiMnAl x alloys. Scr Mater. 2017;138:92-5.
[19] Wang Y, Curtarolo S, Jiang C, Arroyave R, Wang T, Ceder G, et al. Ab initio lattice stability in comparison with CALPHAD lattice stability. Calphad. 2004;28(1):79-90.
[20] Labusch R. A Statistical Theory of Solid Solution Hardening. Phys Status Solidi B. 1970;41(2):659-69.
[21] Li M, Guo Y, Wang H, Shan J, Chang Y. Microstructures and mechanical properties of oxide dispersion strengthened CoCrFeNi high-entropy alloy produced by mechanical alloying and spark plasma sintering. Intermetallics. 2020;123:106819.
[22] Habibnejad-Korayem M, Mahmudi R, Poole WJ. Enhanced properties of Mg-based nano-composites reinforced with Al2O3 nano-particles. Mater Sci Eng A. 2009;519(1):198-203.
[23] Bai K, Lin M. Unravelling the metal borides evolution in the transient liquid phase bonding of Ni-based alloys via high-throughput transmission electron microscopy and first-principles thermo-kinetic calculations. J Mater Sci Technol. 2021;85:118-28.
[24] KUMA P. STUDIES OF WIRE-MATRIX INTERACTION IN SOME TUNGSTEN WIRE REINFORCED STAINLESS STEELS, PH.D Thesis.: University of Canterbury; 2013.
[25] Sun Z, Tan X, Descoins M, Mangelinck D, Tor S, Lim C. Revealing hot tearing mechanism for an additively manufactured high-entropy alloy via selective laser melting. Scr Mater. 2019;168:129-33.
[26] Jayaraj Radhakrishnan R, Kumar P, Seet HL, Nai SML, Wang P, Ramamurty U. Cascading of the as-built microstructure through heat treatment and its role on the tensile properties of laser powder bed fused Inconel 718. Materialia. 2022;21:101272.
[27] Sun Z, Tan X, Tor SB, Chua CK. Simultaneously enhanced strength and ductility for 3D-printed stainless steel 316L by selective laser melting. NPG Asia Mater. 2018;10(4):127-36.
[28] Kim Y-K, Yang S, Lee K-A. Superior Temperature-Dependent Mechanical Properties and Deformation Behavior of Equiatomic CoCrFeMnNi High-Entropy Alloy Additively Manufactured by Selective Laser Melting. Sci Rep. 2020;10(1):8045.
[29] Rehman Hu, Durst K, Neumeier S, Parsa AB, Kostka A, Eggeler G, et al. Nanoindentation studies of the mechanical properties of the μ phase in a creep deformed Re containing nickel-based superalloy. Mater Sci Eng A. 2015;634:202-8.
[30] Liu WH, Lu ZP, He JY, Luan JH, Wang ZJ, Liu B, et al. Ductile CoCrFeNiMox high entropy alloys strengthened by hard intermetallic phases. Acta Mater. 2016;116:332-42.
[31] Yin F, Sakurai A, Song X. Determination of spatial grain size with the area-weighted grain area distribution of the planar sections in polycrystalline materials. Metall Mater Trans A. 2006;37(12):3707-14.

[32] Zhang K, Wang S, Liu W, Shang X. Characterization of stainless steel parts by Laser Metal Deposition Shaping. Mater Des. 2014;55:104-19.
[33] Ziętala M, Durejko T, Polański M, Kunce I, Płociński T, Zieliński W, et al. The microstructure, mechanical properties and corrosion resistance of 316L stainless steel fabricated using laser engineered net shaping. Mater Sci Eng A. 2016;677:1-10.
[34] Wang Z, Palmer TA, Beese AM. Effect of processing parameters on microstructure and tensile properties of austenitic stainless steel 304L made by directed energy deposition additive manufacturing. Acta Mater. 2016;110:226-35.
[35] Mukherjee M. Effect of build geometry and orientation on microstructure and properties of additively manufactured 316L stainless steel by laser metal deposition. Materialia. 2019;7:100359.
[36] Chang R, Fang W, Bai X, Xia C, Zhang X, Yu H, et al. Effects of tungsten additions on the microstructure and mechanical properties of CoCrNi medium entropy alloys. J Alloys Compd. 2019;790:732-43.
[37] Ma MT, Kim DG, Wang GY, Liu G. The Influence of Pre-compression Deformation on Tension Property of DP590. Advanced High Strength Steel and Press Hardening. p. 152-8.
[38] Wu Z, Gao Y, Bei H. Thermal activation mechanisms and Labusch-type strengthening analysis for a family of high-entropy and equiatomic solid-solution alloys. Acta Mater. 2016;120:108-19.
[39] Peyrouzet F, Hachet D, Soulas R, Navone C, Godet S, Gorsse S. Selective Laser Melting of Al0.3CoCrFeNi High-Entropy Alloy: Printability, Microstructure, and Mechanical Properties. JOM. 2019;71(10):3443-51.
[40] Lin D, Xu L, Jing H, Han Y, Zhao L, Minami F. Effects of annealing on the structure and mechanical properties of FeCoCrNi high-entropy alloy fabricated via selective laser melting. Addit Manuf. 2020;32:101058.
[41] Vaidya M, Trubel S, Murty BS, Wilde G, Divinski SV. Ni tracer diffusion in CoCrFeNi and CoCrFeMnNi high entropy alloys. J Alloys Compd. 2016;688:994-1001.
[42] Gaertner D, Kottke J, Chumlyakov Y, Hergemöller F, Wilde G, Divinski S. Tracer diffusion in single crystalline CoCrFeNi and CoCrFeMnNi high-entropy alloys: Kinetic hints towards a low-temperature phase instability of the solid-solution? Scr Mater. 2020;187:57-62.
[43] Dąbrowa J, Danielewski M. State-of-the-Art Diffusion Studies in the High Entropy Alloys. Metals. 2020;10(3):347.
[44] Zhang C, Zhang F, Jin K, Bei H, Chen S, Cao W, et al. Understanding of the Elemental Diffusion Behavior in Concentrated Solid Solution Alloys. J Phase Equilibria Diffus. 2017;38(4):434-44.
[45] Wang J, Lu X-G, Zhu N, Zheng W. Thermodynamic and diffusion kinetic studies of the Fe-Co system. Calphad. 2017;58:82-100.

[46] Liu Y, Zhang L, Du Y, Wang J, Liang D. Study of atomic mobilities and diffusion characteristics in bcc Ti–Ta and Ta–W alloys. Calphad. 2010;34(3):310-6.
[47] Liu D, Zhang L, Du Y, Jin Z. Simulation of atomic mobilities, diffusion coefficients and diffusion paths in bcc_A2 and bcc_B2 phases of the Al–Ni–Fe system. J Alloys Compd. 2015;634:148-55.
[48] Divya VD, Ramamurty U, Paul A. Interdiffusion and Growth of the Phases in CoNi/Mo and CoNi/W Systems. Metall Mater Trans A. 2012;43(5):1564-77.